The Astrophysical Journal, 949:84 (6pp), 2023 June 1 https://doi.org/10.3847/1538-4357/acc9a8

Hanle Effect with Angle-dependent Partial Frequency Redistribution in Three-dimensional Media

L. S. Anusha
Indian Institute of Astrophysics, Koramangala, 2nd Block, Bangalore 560 034, India; anusha.ls@iiap.res.in
Received 2023 January 27; revised 2023 March 28; accepted 2023 March 30; published 2023 June 1

Abstract

There has been a constant improvement in the observational measurement of linear polarization in chromospheric spectral lines in the last three decades. However, modeling polarized profiles of these lines still remains incomplete, due to the lack of inclusion of fundamental physics in modeling efforts. To model the observed solar spectrum and its linear polarization, we need a solution to the polarized radiative transfer equation. The polarization in strong resonance lines originates from the scattering mechanism known as the partial frequency redistribution (PFR) of an anisotropic radiation field. The understanding of the linear polarization in spatially resolved structures needs radiative transfer solutions in multidimensional geometries. In this paper, we explore the effects of angle-dependent PFR on scattering polarization profiles formed in three-dimensional (3D) media. We find that the 3D geometry combined with angle-dependent PFR produces more scattering polarization than an angle-averaged one.

Unified Astronomy Thesaurus concepts: Radiative transfer (1335); Solar atmosphere (1477); Magnetic fields (994)

1. Introduction

The observed linear scattering polarization profiles of the strong resonance lines such as Ca I 4227 Å and Ca II K formed in the solar atmosphere have a characteristic triple-peak structure. It is now established that the theory of partial frequency redistribution (PFR) is necessary to explain this structure (see, e.g., Holzreuter et al. 2005). Angle-dependent PFR is a general theory that includes the coupling between the angles and frequencies of the incident and scattered photons. However, radiative transfer calculations including this general theory are computationally very demanding. Therefore, for modeling the observed polarized profiles an approximation of averaging the PFR functions over the angles (the angle-averaged PFR) is usually adopted.

In the cores of the strong resonance lines, the polarization is also modified by weak magnetic fields (the Hanle effect). Therefore, modeling these lines requires a PFR theory that includes the Hanle effect. The PFR line formation theory with the Hanle effect was first developed by Omont et al. (1972, 1973). An explicit calculation of the PFR matrices for resonance scattering polarization was performed by Domke & Hubeny (1988). Magnetic fields were included by Bommier (1997a, 1997b) to derive Hanle PFR matrices for a two-level atom case using a quantum electrodynamic approach. Recently, Bommier (2016a, 2016b, 2017) extended the PFR theory to a multilevel atom system.

In Anusha & Nagendra (2011a), a historical account of the literature on radiative transfer with angle-dependent PFR is presented. Here, we highlight some of the recent developments. The angle-dependent PFR effects on the polarized spectrum in the context of arbitrary strength magnetic fields and hyperfine structure transition under the incomplete Paschen–Back effect regime have been studied respectively in Sampoorna et al. (2017) and Nagendra et al. (2020). Janett et al. (2021) explored the effect of angle-dependent PFR on the polarization profile of the Ca I 4227 Å line in one-dimensional (1D) empirical model atmospheres.

In a series of papers, we have studied the effect of PFR on the polarized line formation in multidimensional (multi-D) media. Anusha & Nagendra (2011b) and Anusha & Nagendra (2011c) were dedicated to understanding the effects of angle-averaged PFR on the scattering polarization profiles in nonmagnetic and magnetic media. Angle-dependent PFR effects in two-dimensional (2D) media are explored in Anusha & Nagendra (2011a) and Anusha & Nagendra (2012). The implementation was restricted to radiative transfer in 2D due to the limited computational resources. To model polarization observations using three-dimensional (3D) magnetohydrodynamic (MHD) models of the solar chromosphere (see, e.g., Przybylski et al. 2022), we need 3D polarized radiative transfer solutions. Prior to undertaking the numerically expensive modeling efforts, it is essential to understand the 3D results in simple model atmospheres. Therefore, in this paper, for the first time, we solve the polarized 3D radiative transfer equation with angle-dependent PFR and present benchmark results.

2. Polarized Transfer with Angle-dependent PFR

The non–local thermodynamic equilibrium (non-LTE) polarized transfer equation is a coupled nonlinear problem. The nonlinearity of the non-LTE polarized transfer equation is due to the coupling between the statistical equilibrium equation for the atomic energy levels and the radiative transfer equation (see, e.g., Landi Degl'Innocenti & Landolfi 2004, chapter 6). The nonlocality arises due to the coupling of the angles, frequencies, and spatial points. We limit our formalism in this paper to a two-level atom model with unpolarized ground level. Therefore, the transfer equation considered here (Equation (1)) is a nonlocal, linear equation, which is complex to solve. When angle-dependent PFR scattering is included, the angular dependence in the source and the Stokes vectors further complicates the problem. The decomposition technique developed in Anusha & Nagendra (2011a, 2012) addresses the solution in multi-D geometry, posing the problem in an irreducible spherical tensor formalism combined

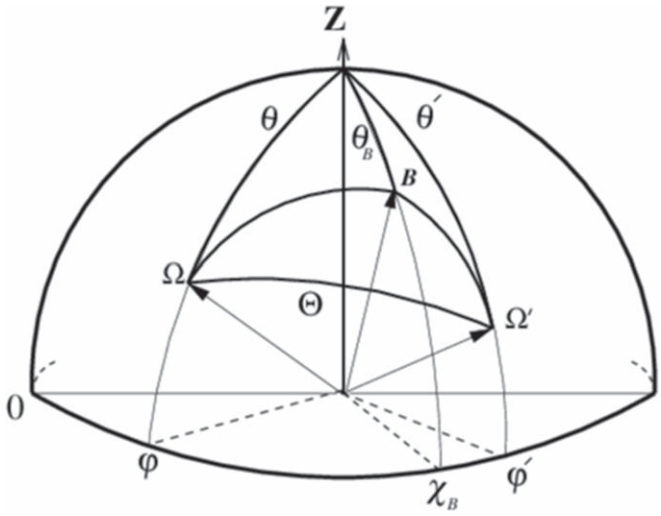

Figure 1. The atmospheric reference frame. The outgoing ray direction is defined by the angle pair (θ, φ). $\boldsymbol{B} = (\Gamma, \theta_B, \chi_B)$ represents the magnetic field vector, where Γ is the Hanle efficiency parameter and (θ_B, χ_B) defines the field direction. The scattering angle is marked as Θ.

with Fourier series expansion. All the symbols and notations used in this paper are the same as in Anusha & Nagendra (2012). Therefore, we do not repeat their description. We give the basic equations here.

Let us consider a multi-D medium with an oriented magnetic field $\boldsymbol{B}$ (see Figure 1). The polarized transfer equation for a given ray defined by direction $\boldsymbol{\Omega}$ at a position vector $\boldsymbol{r} = (x, y, z)$ is given by

$$\boldsymbol{\Omega} \cdot \boldsymbol{\nabla} \boldsymbol{I}(\boldsymbol{r}, \boldsymbol{\Omega}, x, \boldsymbol{B}) = -[\kappa_l(\boldsymbol{r})\phi(x) + \kappa_c(\boldsymbol{r})] \times [\boldsymbol{I}(\boldsymbol{r}, \boldsymbol{\Omega}, x, \boldsymbol{B}) - \boldsymbol{S}(\boldsymbol{r}, \boldsymbol{\Omega}, x, \boldsymbol{B})], \quad (1)$$

where $\boldsymbol{I} = (I, Q, U)^T$ is the Stokes vector, with I, Q, and U the Stokes parameters (see, e.g., Chandrasekhar 1960, for a definition). The solid angle element is defined as $d\boldsymbol{\Omega}' = \sin\theta'\, d\theta'\, d\varphi'$, where $\theta \in [0, \pi]$ and $\varphi \in [0, 2\pi]$. The direction cosines of the ray are $\boldsymbol{\Omega} = (\eta, \gamma, \mu) = (\sin\theta\cos\varphi, \sin\theta\sin\varphi, \cos\theta)$, with θ and φ being the polar and azimuthal angles of the ray (see Figure 1).

Here, κ_l and κ_c are line and continuum opacities, respectively, with ϕ being the Voigt profile function. $x = (\nu - \nu_0)/\Delta\nu_D$ is the frequency measured in reduced units, with $\Delta\nu_D$ being the Doppler width. The source vector is given by

$$\boldsymbol{S}(\boldsymbol{r}, \Omega, x, \boldsymbol{B}) = \frac{\kappa_l(\boldsymbol{r})\phi(x)\boldsymbol{S}_l(\boldsymbol{r}, \Omega, x, \boldsymbol{B}) + \kappa_c(\boldsymbol{r})\boldsymbol{S}_c(\boldsymbol{r}, x)}{\kappa_l(\boldsymbol{r})\phi(x) + \kappa_c(\boldsymbol{r})}. \quad (2)$$

Here, $\boldsymbol{S}_c(\boldsymbol{r}, x) = (B_\nu(\boldsymbol{r}), 0, 0)^T$ is the unpolarized continuum source vector, with $B_\nu(\boldsymbol{r})$ being the Planck function. The line source vector is

$$\boldsymbol{S}_l(\boldsymbol{r}, \boldsymbol{\Omega}, x, \boldsymbol{B}) = \boldsymbol{G}(\boldsymbol{r}) + \int_{-\infty}^{+\infty} dx' \times \oint \frac{d\boldsymbol{\Omega}'}{4\pi} \frac{\hat{R}(x, x', \boldsymbol{\Omega}, \boldsymbol{\Omega}', \boldsymbol{B})}{\phi(x)} \boldsymbol{I}(\boldsymbol{r}, \boldsymbol{\Omega}', x', \boldsymbol{B}), \quad (3)$$

where the thermal source vector is $\boldsymbol{G}(\boldsymbol{r}) = \epsilon \boldsymbol{B}_\nu(\boldsymbol{r})$ with $\boldsymbol{B}_\nu(\boldsymbol{r}) = (B_\nu(\boldsymbol{r}), 0, 0)^T$, and $\hat{R}$ is the Hanle redistribution matrix with angle-dependent PFR (see Section 4.2, approximation II, of Bommier 1997b). We recall here that the matrix $\hat{R}$ involves the destruction probability per scattering ϵ and the damping parameter a of the Voigt profile function. Here, $\epsilon = \Gamma_I/(\Gamma_R + \Gamma_I)$, with Γ_I and Γ_R being the inelastic collision rate and the radiative de-excitation rate, respectively. The damping parameter $a = a_R[1 + (\Gamma_E + \Gamma_I)/\Gamma_R]$, with $a_R = \Gamma_R/4\pi\Delta\nu_D$ and Γ_E being the elastic collision rate.

3. Transfer Equation in Terms of Irreducible Spherical Tensors

Frisch (2007) showed that, for a 1D planar geometry, $\boldsymbol{S}$ and $\boldsymbol{I}$ can be decomposed into irreducible vectors $\boldsymbol{S}$ and $\boldsymbol{I}$ of dimension six each, defined as

$$\boldsymbol{S} = (S_0^0, S_0^2, S_1^{2,x}, S_1^{2,y}, S_2^{2,x}, S_2^{2,y})^T,$$
$$\boldsymbol{I} = (I_0^0, I_0^2, I_1^{2,x}, I_1^{2,y}, I_2^{2,x}, I_2^{2,y})^T. \quad (4)$$

A generalization of the above techniques to the multi-D case was developed and presented in Anusha & Nagendra (2011b, 2011c). It was shown that $\boldsymbol{I}$ and $\boldsymbol{I}$ satisfy a transfer equation of the form

$$-\frac{1}{\kappa_{\rm tot}(\boldsymbol{r}, x)} \boldsymbol{\Omega} \cdot \boldsymbol{\nabla} \boldsymbol{I}(\boldsymbol{r}, \boldsymbol{\Omega}, x, \boldsymbol{B}) = [\boldsymbol{I}(\boldsymbol{r}, \boldsymbol{\Omega}, x, \boldsymbol{B}) - \boldsymbol{S}(\boldsymbol{r}, \boldsymbol{\Omega}, x, \boldsymbol{B})], \quad (5)$$

where $\kappa_{\rm tot}$ is the sum of the line and continuum opacities and is given by $\kappa_{\rm tot}(\boldsymbol{r}, x) = \kappa_l(\boldsymbol{r})\phi(x) + \kappa_c(\boldsymbol{r})$, and

$$\boldsymbol{S}(\boldsymbol{r}, \boldsymbol{\Omega}, x, \boldsymbol{B}) = p_x \boldsymbol{S}_l(\boldsymbol{r}, \boldsymbol{\Omega}, x, \boldsymbol{B}) + (1 - p_x)\boldsymbol{S}_C(\boldsymbol{r}, x), \quad (6)$$

with the ratio of the line opacity to the total opacity being given by

$$p_x = \kappa_l(\boldsymbol{r})\phi(x)/\kappa_{\rm tot}(\boldsymbol{r}, x). \quad (7)$$

The irreducible line source vector is given by

$$\boldsymbol{S}_l(\boldsymbol{r}, \boldsymbol{\Omega}, x, \boldsymbol{B}) = \boldsymbol{G}(\boldsymbol{r}) + \frac{1}{\phi(x)} \int_{-\infty}^{+\infty} dx' \times \oint \frac{d\boldsymbol{\Omega}'}{4\pi} \{\hat{M}_{\rm II}(\boldsymbol{B}, x, x') r_{\rm II}(x, x', \boldsymbol{\Omega}, \boldsymbol{\Omega}') + \hat{M}_{\rm III}(\boldsymbol{B}, x, x') r_{\rm III}(x, x', \boldsymbol{\Omega}, \boldsymbol{\Omega}')\} \hat{\Psi}_W(\boldsymbol{\Omega}') \times \boldsymbol{I}(\boldsymbol{r}, \boldsymbol{\Omega}', x', \boldsymbol{B}), \quad (8)$$

where $\hat{\Psi}_W(\boldsymbol{\Omega}') = \sqrt{\hat{W}}\hat{\Psi}(\boldsymbol{\Omega}')\sqrt{\hat{W}}$ (see chapter 14 in Frisch 2022). Here, the atomic depolarization parameter is represented by the matrix $\hat{W} = {\rm diag}\{W_0, W_2, W_2, W_2, W_2, W_2\}$ and $\hat{\Psi}$ is a 6x6 matrix that represents the reduced Rayleigh scattering phase matrix, whose elements can be found in several papers (see, e.g., Appendix D in Anusha & Nagendra 2011c). The unpolarized continuum source vector is denoted as $\boldsymbol{G}(\boldsymbol{r}) = \epsilon \boldsymbol{B}_\nu(\boldsymbol{r})$, with $\boldsymbol{B}_\nu(\boldsymbol{r}) = (B_\nu(\boldsymbol{r}), 0, 0, 0, 0, 0)^T$. The redistribution matrix consists of the well-known angle-dependent PFR functions $r_{\rm II,III}$ (see Hummer 1962) and frequency-domain-dependent Hanle phase matrices $\hat{M}_{\rm II,III}(\boldsymbol{B}, x, x')$ (see Bommier 1997a, 1997b). The redistribution functions depend explicitly on the scattering angle Θ (see Figure 1), defined by $\cos\Theta = \boldsymbol{\Omega} \cdot \boldsymbol{\Omega}'$, which can be written as

$$\cos\Theta = \mu\mu' + \sqrt{(1 - \mu^2)(1 - \mu'^2)}\cos(\varphi' - \varphi). \quad (9)$$

The expression for the matrices $\hat{M}_{\rm II,III}(\boldsymbol{B}, x, x')$ can be found in several references (see, e.g., Anusha & Nagendra 2011c). For all other notations and symbols, we refer the reader to Anusha & Nagendra (2011a, 2012).

3.1. Reduced Transfer Equation Using Fourier Decomposition

A further reduction of the irreducible Stokes and the source vectors in terms of a Fourier series expansion to simplify the radiative transfer problem with angle-dependent PFR was introduced in Frisch (2010). A generalization of the same, to multi-D geometry, is presented in Anusha & Nagendra (2011a, 2012). The angle-dependent PFR matrix with the Hanle effect has the form

$$\begin{aligned}&\hat{R}(x, x', \boldsymbol{\Omega}, \boldsymbol{\Omega}', \boldsymbol{B})\\&= \{\hat{M}_{\rm II}(\boldsymbol{B}, x, x') r_{\rm II}(x, x', \boldsymbol{\Omega}, \boldsymbol{\Omega}')\\&\quad + \hat{M}_{\rm III}(\boldsymbol{B}, x, x') r_{\rm III}(x, x', \boldsymbol{\Omega}, \boldsymbol{\Omega}')\}\hat{\Psi}_W(\boldsymbol{\Omega}'). \qquad (10)\end{aligned}$$

The Fourier series expansions of the functions $r_{\rm II,\,III}(x, x', \boldsymbol{\Omega}, \boldsymbol{\Omega}')$ is written as

$$\begin{aligned}&r_{\rm II,III}(x, x', \boldsymbol{\Omega}, \boldsymbol{\Omega}')\\&= \sum_{k=0}^{k=\infty} (2 - \delta_{k0}) e^{ik\varphi}\, \tilde{r}^{(k)}_{\rm II,III}(x, x', \theta, \boldsymbol{\Omega}'), \qquad (11)\end{aligned}$$

with

$$\begin{aligned}&\tilde{r}_{\rm II,III}{}^{(k)}(x, x', \theta, \boldsymbol{\Omega}') = \int_0^{2\pi} \frac{d\,\varphi}{2\pi}\, e^{-ik\varphi}\\&\times r_{\rm II,III}(x, x', \boldsymbol{\Omega}, \boldsymbol{\Omega}'). \qquad (12)\end{aligned}$$

Substituting Equation (11) in Equation (10), we can write the ijth element of the $\hat{R}$ matrix as

$$\begin{aligned}&R_{ij}(x, x', \boldsymbol{\Omega}, \boldsymbol{\Omega}', \boldsymbol{B})\\&= \sum_{k=0}^{k=\infty} (2 - \delta_{k0}) e^{ik\varphi}\, \tilde{R}^{(k)}_{ij}(x, x', \theta, \boldsymbol{\Omega}', \boldsymbol{B}),\\&\quad i, j = 1, 2, \ldots, 6, \qquad (13)\end{aligned}$$

where $\tilde{R}^{(k)}_{ij}$ are

$$\begin{aligned}&\tilde{R}^{(k)}_{ij}(x, x', \theta, \boldsymbol{\Omega}') = \int_0^{2\pi} \frac{d\,\varphi}{2\pi}\, e^{-ik\varphi}\\&\{(\hat{M}_{\rm II})_{ij}(\boldsymbol{B}, x, x') r_{\rm II}(x, x', \boldsymbol{\Omega}, \boldsymbol{\Omega}')\\&\quad + (\hat{M}_{\rm III})_{ij}(\boldsymbol{B}, x, x') r_{\rm III}(x, x', \boldsymbol{\Omega}, \boldsymbol{\Omega}')\}(\Psi_W)_{ij}. \qquad (14)\end{aligned}$$

Applying this expansion, we can derive a polarized radiative transfer equation in terms of the Fourier coefficients $\tilde{\boldsymbol{I}}^{(k)}$ and $\tilde{\boldsymbol{S}}^{(k)}$, namely

$$\begin{aligned}&-\frac{1}{\kappa_{\rm tot}(\boldsymbol{r}, x)} \boldsymbol{\Omega} \cdot \boldsymbol{\nabla} \tilde{\boldsymbol{I}}^{(k)}(\boldsymbol{r}, \boldsymbol{\Omega}, x)\\&= [\tilde{\boldsymbol{I}}^{(k)}(\boldsymbol{r}, \boldsymbol{\Omega}, x) - \tilde{\boldsymbol{I}}^{(k)}(\boldsymbol{r}, \theta, x)], \qquad (15)\end{aligned}$$

where

$$\begin{aligned}&\boldsymbol{S}(\boldsymbol{r}, \boldsymbol{\Omega}, x)\\&= \sum_{k=0}^{k=\infty} (2 - \delta_{k0}) \{\cos(k\varphi) Re[\tilde{\boldsymbol{S}}^{(k)}(\boldsymbol{r}, \theta, x)]\\&- \sin(k\varphi) Im[\tilde{\boldsymbol{S}}^{(k)}(\boldsymbol{r}, \theta, x)]\}, \qquad (16)\end{aligned}$$

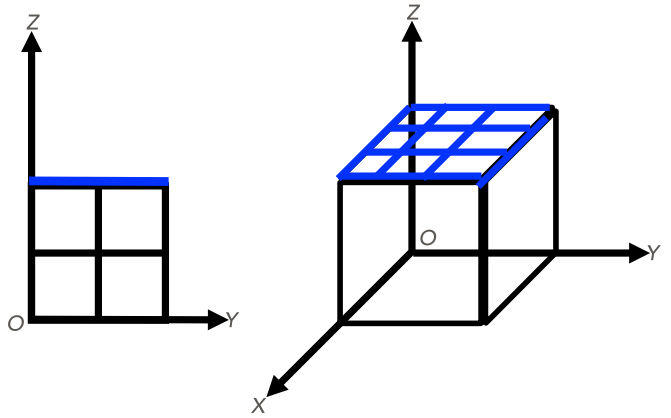

Figure 2. The figure shows cartoon diagrams of the 2D slab (left) and 3D box (right) atmospheres considered for the radiative transfer computations presented in this paper. The areas marked as blue represent the regions considered for the spatial averaging of the emergent solutions shown in Section 4.

and

$$\begin{aligned}&\boldsymbol{I}(\boldsymbol{r}, \boldsymbol{\Omega}, x)\\&= \sum_{k=0}^{k=\infty} (2 - \delta_{k0}) \{\cos(k\varphi) Re[\tilde{\boldsymbol{I}}^{(k)}(\boldsymbol{r}, \boldsymbol{\Omega}, x)]\\&- \sin(k\varphi) Im[\tilde{\boldsymbol{I}}^{(k)}(\boldsymbol{r}, \boldsymbol{\Omega}, x)]\}. \qquad (17)\end{aligned}$$

Equation (15) represents the most reduced form of the polarized radiative transfer equation in multi-D geometry with the angle-dependent PFR. Hereafter, we refer to $\tilde{\boldsymbol{I}}^{(k)}$ and $\tilde{\boldsymbol{S}}^{(k)}$ as "irreducible Fourier coefficients." $\tilde{\boldsymbol{I}}^{(k)}$ and $\tilde{\boldsymbol{S}}^{(k)}$ are six-dimensional complex vectors for each value of k.

4. Results and Discussions

In this section, we present the solutions of the 2D and 3D polarized radiative transfer equations with the PFR scattering mechanism. We compare the results computed in 2D and 3D media using angle-averaged and angle-dependent PFR. We adopt an idealized atmosphere that is a magnetized 2D slab or a 3D box (see Figure 2), with a total optical thickness of 20 in each direction. The magnetic field vector $\boldsymbol{B} = (\Gamma, \theta_B, \chi_B) = (1, 90°, 60°)$. The branching ratios of the PFR matrices are chosen such that they represent the collisionless redistribution process case that uses only the $\tilde{r}_{\rm II}{}^{(k)}(x, x', \theta, \boldsymbol{\Omega}')$ function. For the numerical calculations in this paper, we keep five Fourier components. We choose the damping parameter of the Voigt profile function $a = 10^{-3}$, and the ratios of the elastic and inelastic collision rates to the radiative de-excitation rate are, respectively, $\Gamma_E/\Gamma_R = 10^{-4}$ and $\Gamma_I/\Gamma_R = 10^{-4}$. All other global parameters are the same as in Anusha & Nagendra (2012).

The Krylov space iterative method preconditioned stabilized biconjugate gradient is used here as the numerical method for solving the polarized radiative transfer equation. As described in Anusha et al. (2009), this method is much faster compared to other state-of-the-art numerical methods. The adaptation of this method to polarized transfer with PFR in multi-D media is presented in detail in our previous papers (Anusha & Nagendra 2011c, 2012).

In Figures 3 and 4, we show Q/I and U/I profiles for $\mu = 0.11$ and 16 φ values. In these figures, we compare the polarized profiles computed with the angle-averaged and the

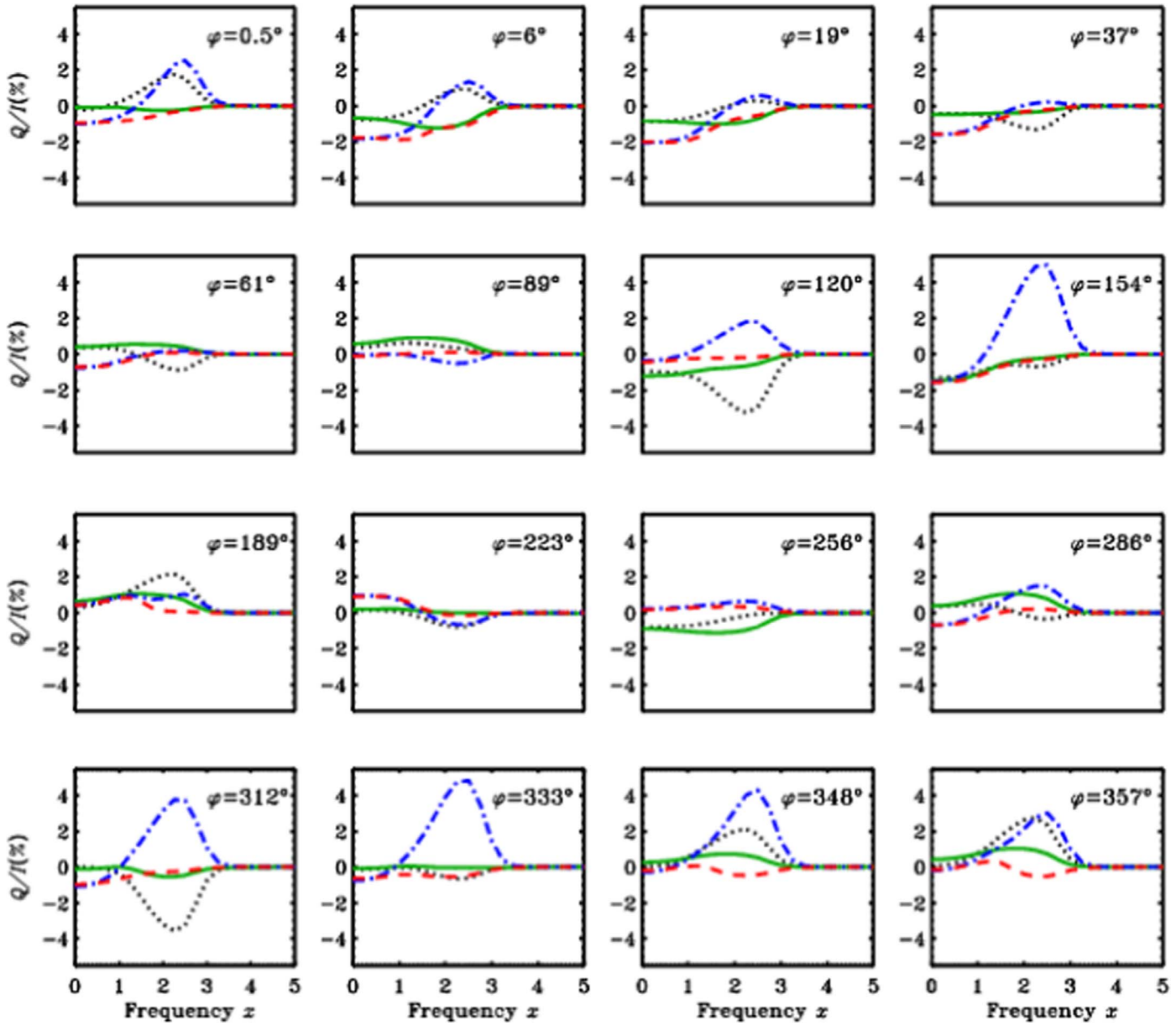

Figure 3. The figure shows the Hanle effect with PFR in multi-D media. We plot the emergent, spatially averaged Q/I profiles with angle-averaged PFR in 2D and 3D media (the dashed and solid lines, respectively) and angle-dependent PFR in 2D and 3D media (the dotted–dashed and dotted lines, respectively). The Q/I profiles are along a line of sight of $\mu = 0.11$ and 16 different φ values that are marked in the respective panels.

angle-dependent PFR in magnetized 2D and 3D media. For the optical thickness considered here, the PFR effects are restricted to $0 \leqslant x \leqslant 5$. The 2D profiles are the same as in Figures 7 and 8 of Anusha & Nagendra (2012). We recall the discussions in that paper that the shapes of the angle-dependent polarization profiles are quite different from those of the angle-averaged profiles in the magnetic case, while the differences were marginal in the nonmagnetic case. We see a similar trend in the 3D case as well. The angle-dependent profiles are peaked around $x = 2.5$ in both the 2D and 3D media for most φ values, while the angle-averaged profiles are rather flat. Further, the angle-dependent PFR modifies the polarization profiles predominantly in the line core ($0 \leqslant x \leqslant 3.5$). This is because the presence of the magnetic field modifies the polarization due to scattering via the Hanle effect, which operates only in the line core. In particular, it is the Hanle effect that brings out the importance of the angle-dependent PFR.

A comparison of the polarization profiles in 2D and 3D media shows that they are sensitive to the orientation (θ, φ) of the line of sight. In the angle-dependent case, $|Q/I|$ ($|U/I|$) reaches a maximum magnitude of $\sim$5% (4%) and $\sim$3.5% (3.8%), respectively, in 2D and 3D media. Thus, the 3D medium reaches a lower maximum magnitude in comparison to the 2D medium. This is because in the 3D medium, there is a larger area over which the spatial averaging is carried out on the sign-changing quantities.

In Figure 5, we show the μ variation of the emergent, spatially averaged (Log I, Q/I, U/I) profiles computed using angle-dependent PFR in a 3D medium. For the chosen optical thickness of the atmosphere, log I is relatively less sensitive to the orientation of the line of sight when compared to the

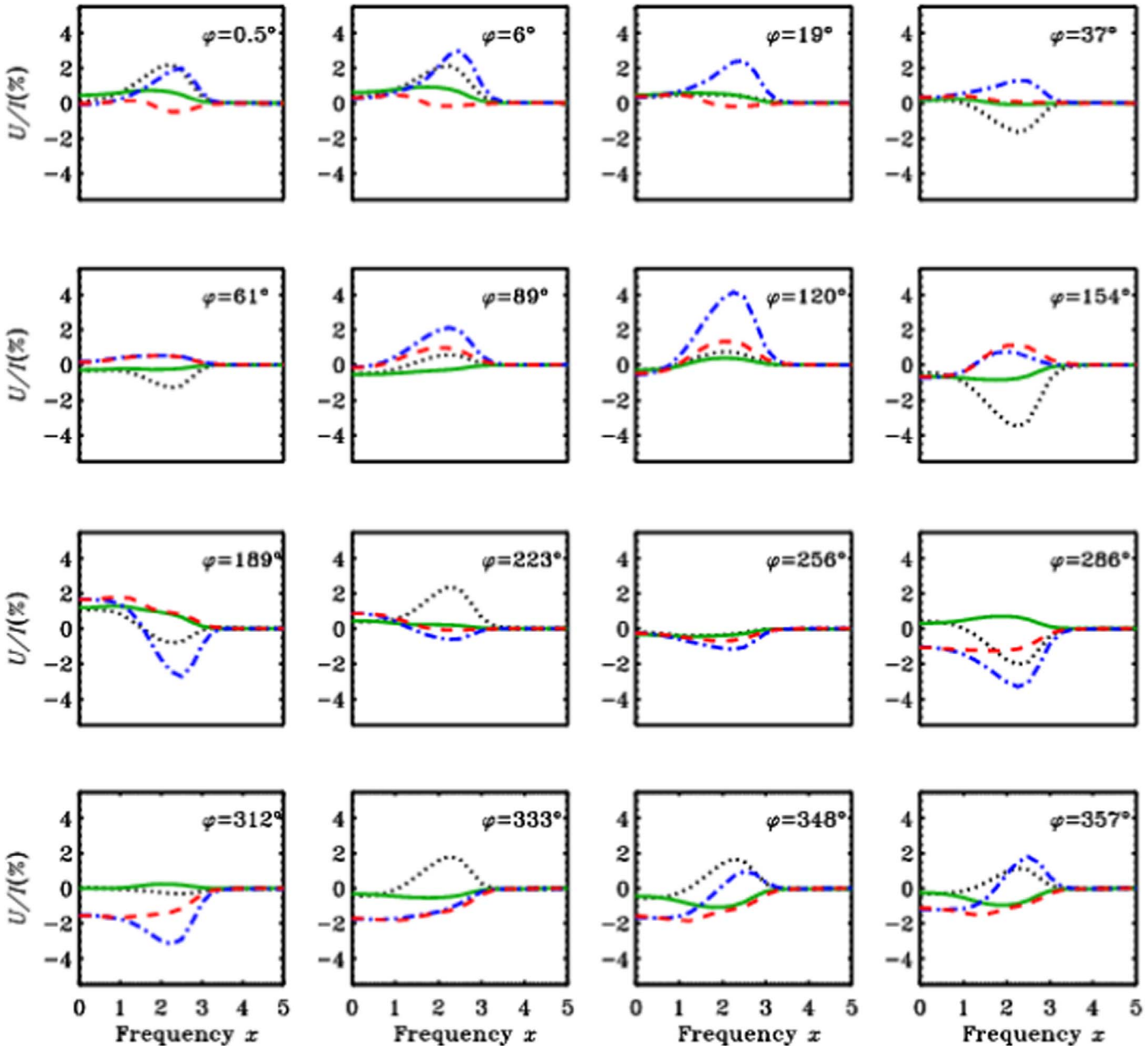

Figure 4. The same as Figure 3, but for U/I profiles.

polarization profiles. For the φ values shown here, the peak values of $|Q/I|$ and $|U/I|$ are, respectively, around 4% and 2.5%.

5. Conclusions

In this paper, we have studied the effects of angle-dependent PFR on polarized line formation and the Hanle effect in 3D media. As already established in 1D (Nagendra et al. 2002) and 2D media (Anusha & Nagendra 2011a, 2012), the 3D geometry combined with angle-dependent PFR and the Hanle effect produces significant scattering polarization. The approximation of angle averaging is not a good representation of the PFR functions. This is reflected in the Q/I and U/I profiles. Qualitatively, the angle-dependent PFR effects in 2D and 3D media are similar. However, quantitatively, the differences are remarkable.

Radiative transfer in multi-D media in general is very demanding. The inclusion of angle-dependent PFR further increases the demand. However, it is important to study the effect of angle-dependent PFR in 3D media in comparison to the approximations of a medium that is 1D or 2D. The computation time for the 3D results presented in this paper was around one week, using a 64 bit Intel Xeon CPU E5-2630 v4 at 2.20 GHz. We conclude that the differences that angle-dependent PFR manifests in polarized line profiles make it a necessary mechanism to be implemented in the 3D modeling of polarization observations. In particular, it is worthwhile to explore the effects of the angle-dependent PFR in modeling strong resonance lines, such as Ca I 4227 Å, in 3D MHD model atmospheres. This requires faster numerical techniques to be developed and implemented to address the computational demands.

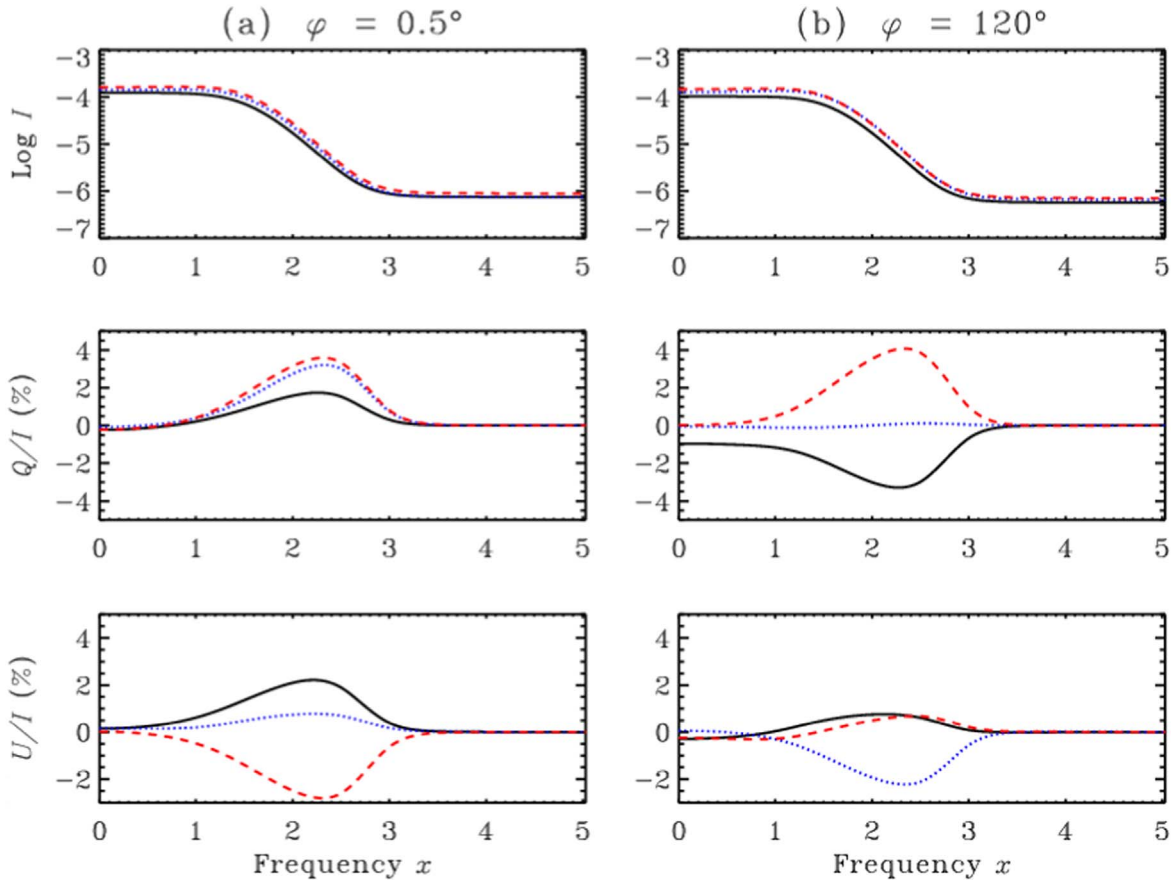

Figure 5. The figure shows the angular variation of the Hanle effect in 3D media with angle-dependent PFR. We plot the emergent, spatially averaged Log I, Q/I, and U/I profiles. The solid, dotted, and dotted–dashed lines represent $\mu = (0.11, 0.5, 0.88)$, respectively. Panel (a) corresponds to $\varphi = 0.^{\circ}5$ and panel (b) to $\varphi = 120^{\circ}$.

The author thanks Prof. Helene Frisch for useful discussions and Dr. L. S. Sharath Chandra for critical reading of the manuscript. The author thanks the HPC facility at the Indian Institute of Astrophysics that was used to compute the results presented in this paper.

References

Anusha, L. S., & Nagendra, K. N. 2011a, ApJ, 739, 40
Anusha, L. S., & Nagendra, K. N. 2011b, ApJ, 726, 6
Anusha, L. S., & Nagendra, K. N. 2011c, ApJ, 738, 116
Anusha, L. S., & Nagendra, K. N. 2012, ApJ, 746, 84
Anusha, L. S., Nagendra, K. N., Paletou, F., & Léger, L. 2009, ApJ, 704, 661
Bommier, V. 1997a, A&A, 328, 706
Bommier, V. 1997b, A&A, 328, 726
Bommier, V. 2016a, A&A, 591, A59
Bommier, V. 2016b, A&A, 591, A60
Bommier, V. 2017, A&A, 607, A50
Chandrasekhar, S. 1960, Radiative Transfer (New York: Dover)
Domke, H., & Hubeny, I. 1988, ApJ, 334, 527
Frisch, H. 2007, A&A, 476, 665
Frisch, H. 2010, A&A, 522, A41
Frisch, H. 2022, Radiative Transfer: An Introduction to Exact and Asymptotic Methods (Cham: Springer)
Holzreuter, R., Fluri, D. M., & Stenflo, J. O. 2005, A&A, 434, 713
Hummer, D. G. 1962, MNRAS, 125, 21
Janett, G., Ballester, E. A., Guerreiro, N., et al. 2021, A&A, 655, A13
Landi Degl'Innocenti, E., & Landolfi, M. 2004, Polarization in Spectral Lines (Dordrecht: Kluwer), 237
Nagendra, K. N., Frisch, H., & Faurobert, M. 2002, A&A, 395, 305
Nagendra, K. N., Sowmya, K., Sampoorna, M., Stenflo, J. O., & Anusha, L. S. 2020, ApJ, 898, 49
Omont, A., Smith, E. W., & Cooper, J. 1972, ApJ, 175, 185
Omont, A., Smith, E. W., & Cooper, J. 1973, ApJ, 182, 283
Przybylski, D., Cameron, R., Solanki, S. K., et al. 2022, A&A, 664, A91
Sampoorna, M., Nagendra, K. N., & Stenflo, J. O. 2017, ApJ, 844, 97